Structural basis of peptidoglycan endopeptidase regulation

Jung-Ho Shin[a,1], Alan G. Sulpizio[a,1], Aaron Kelley[b,1], Laura Alvarez[c], Shannon G. Murphy[a,d], Lixin Fan[e], Felipe Cava[c], Yuxin Mao[a], Mark A. Saper[b], and Tobias Dörr[a,d,f,2]

[a]Weill Institute for Cell and Molecular Biology, Cornell University, Ithaca, NY 14853; [b]Department of Biological Chemistry, University of Michigan, Ann Arbor, MI 48109-5606; [c]The Laboratory for Molecular Infection Medicine Sweden, Department of Molecular Biology, Umeå University, SE-901 87 Umeå, Sweden; [d]Department of Microbiology, Cornell University, Ithaca, NY 14853; [e]Basic Science Program, Frederick National Laboratory for Cancer Research, SAXS Core Facility of the National Cancer Institute, Frederick, MD 21702; and [f]Cornell Institute of Host-Microbe Interactions and Disease, Cornell University, Ithaca, NY 14853

Edited by Lalita Ramakrishnan, University of Cambridge, Cambridge, United Kingdom, and approved March 31, 2020 (received for review January 28, 2020)

Most bacteria surround themselves with a cell wall, a strong meshwork consisting primarily of the polymerized aminosugar peptidoglycan (PG). PG is essential for structural maintenance of bacterial cells, and thus for viability. PG is also constantly synthesized and turned over; the latter process is mediated by PG cleavage enzymes, for example, the endopeptidases (EPs). EPs themselves are essential for growth but also promote lethal cell wall degradation after exposure to antibiotics that inhibit PG synthases (e.g., β-lactams). Thus, EPs are attractive targets for novel antibiotics and their adjuvants. However, we have a poor understanding of how these enzymes are regulated in vivo, depriving us of novel pathways for the development of such antibiotics. Here, we have solved crystal structures of the LysM/M23 family peptidase ShyA, the primary EP of the cholera pathogen *Vibrio cholerae*. Our data suggest that ShyA assumes two drastically different conformations: a more open form that allows for substrate binding and a closed form, which we predicted to be catalytically inactive. Mutations expected to promote the open conformation caused enhanced activity in vitro and in vivo, and these results were recapitulated in EPs from the divergent pathogens *Neisseria gonorrheae* and *Escherichia coli*. Our results suggest that LysM/M23 EPs are regulated via release of the inhibitory Domain 1 from the M23 active site, likely through conformational rearrangement in vivo.

autolysin | M23 | *Vibrio cholerae* | LysM

The bacterial cell wall is essential for growth, shape maintenance, and survival of most free-living bacteria. Due to its vital role in bacterial structural integrity, the cell wall is a time-tested target for our most effective antibiotics and continues to be at the center of drug discovery efforts (1). The major constituent of the bacterial cell wall is peptidoglycan (PG), a complex macromolecule composed of polysaccharide strands that are cross-linked via short oligopeptide side stems to form a mesh-like structure. PG is assembled outside of the cytoplasmic membrane from a lipid-linked disaccharide-pentapeptide precursor called lipid II. During cell wall assembly, lipid II is polymerized via glycosyltransferase activities of class A penicillin-binding proteins (aPBPs) and shape, elongation, division, and sporulation (SEDS) proteins RodA and FtsW. The resulting PG strands are then cross-linked with one another via a transpeptidation reaction catalyzed by the bifunctional aPBPs and by class B penicillin-binding proteins that associate with SEDS proteins (2–7).

Due to its importance in maintaining structural integrity in the face of changing environmental conditions that impose variable osmotic pressures, PG [in gram-negative bacteria in conjunction with the outer membrane (8)] must form a tight and robust cage around the bacterial cell. While maintaining the cell wall's vital structural role, however, the cell must also be able to expand [beyond the limits of what stretching of PG could accomplish (9, 10)], divide, and insert macromolecular protein complexes into its cell envelope. Thus, cell wall synthesis alone is insufficient; PG must also be constantly modified, degraded, and resynthesized. These turnover processes are mediated by a group of enzymes often collectively referred to as "autolysins." Autolysins cleave a variety of bonds in the PG meshwork and, in doing so, fulfill important physiological functions such as shape generation [endopeptidases (EPs) (11, 12)], daughter cell separation [amidases and lytic transglycosylases (LTGs) (13–19)], insertion of transmembrane protein complexes [LTGs, EPs (20–22)], and cell elongation [EPs (23–26)].

Because they can cleave bonds within the PG meshwork, autolysins are potentially as dangerous as they are important, since unchecked cell wall degradation can in principle result in cell lysis and death. Amidases (which cut between polysaccharide backbone and peptide side stem), LTGs (which cleave the PG polysaccharide backbone), and EPs (which cleave the bond between peptide side stems), for example, degrade PG following exposure to β-lactam antibiotics (15, 27–30). This results in cell lysis or the formation of nondividing, cell wall-deficient spheroplasts (27, 31, 32). EPs play a particularly dominant role during antibiotic-induced spheroplast formation, at least in the cholera pathogen *Vibrio cholerae* (27). Autolysins are also often highly

Significance

Bacteria digest their cell wall following exposure to antibiotics like penicillin. The endopeptidases (EPs) are among the proteins that catalyze cell wall digestion processes after antibiotic exposure, but we do not understand how these enzymes are regulated during normal growth. Herein, we present the structure of the major EP from the diarrheal pathogen *Vibrio cholerae*. Surprisingly, we find that EPs from this and other pathogens appear to be produced as a largely inactive precursor that undergoes a conformational shift exposing the active site to engage in cell wall digestion. These results enhance our understanding of how EPs are regulated and could open the door for the development of antibiotics that overactivate cell wall digestion processes.

Author contributions: J.-H.S., A.G.S., A.K., M.A.S., and T.D. designed research; J.-H.S., A.G.S., A.K., L.A., S.G.M., L.F., and T.D. performed research; J.-H.S., A.G.S., A.K., L.F., F.C., Y.M., M.A.S., and T.D. contributed new reagents/analytic tools; J.-H.S., A.G.S., A.K., L.A., S.G.M., L.F., F.C., Y.M., M.A.S., and T.D. analyzed data; and M.A.S. and T.D. wrote the paper.

The authors declare no competing interest.

This article is a PNAS Direct Submission.

Data deposition: The atomic coordinates and structure factors have been deposited in the Protein Data Bank, https://www.rcsb.org/ (PDB ID codes 6UE4 [ShyA^{CLOSED}], and 6U2A [ShyA^{OPEN}]).

[1]J.-H.S., A.G.S., and A.K. contributed equally to this work.

[2]To whom correspondence may be addressed. Email: tdoerr@cornell.edu.

This article contains supporting information online at https://www.pnas.org/lookup/suppl/doi:10.1073/pnas.2001661117/-/DCSupplemental.

First published May 11, 2020.

abundant. *V. cholerae*, for example, encodes nine predicted EPs, of which only ShyA and ShyC are collectively essential for cell elongation (23). Similarly, the model organism *Escherichia coli* encodes at least eight EPs (24, 33, 34). Due to this inherently perilous potential, EPs must be tightly regulated under normal growth conditions to ensure proper PG turnover without compromising structural integrity.

We currently have an incomplete understanding of how EPs are regulated in bacteria. The gram-positive bacterium *Bacillus subtilis* (and likely other gram-positive species as well) regulates EP activity via interactions with FtsEX and the PG synthesis elongation machinery (35–37) and additionally encodes a post-translational negative regulator, IseA (YoeB) (38), which presumably serves to tone down EP activity during cell wall stress conditions (38, 39). Much less is known about EP regulation in gram-negative bacteria, where EPs appear to be kept in check as part of multiprotein complexes (40, 41), at the transcriptional level (42, 43), or via proteolytic degradation (44, 45). Proteolytic turnover appears to be the major mode of regulation of growth-promoting EPs (44, 45); however, phenotypes associated with the accumulation of EPs have surprisingly mild phenotypes under normal growth conditions, suggesting an additional unexplored layer of regulation.

Here, we present two crystal structures of the major EP ShyA of *V. cholerae*. The ShyA structure yielded two drastically different conformations, of which only one appears to be active. We thus propose that EPs are produced in a predominantly inactive form and regulated by stabilizing their active conformation in vivo. Importantly, the domain organization and mechanism of regulation via conformational switching appear to be conserved among diverse gram-negative pathogens. These results expose a mechanism of EP regulation in gram-negative pathogens that could open up avenues for the development of antibiotics that activate EPs to the detriment of bacterial viability.

Results

Genetic Evidence Suggests That LysM/M23 Endopeptidases Are Produced in an Inactive Form. The ability of EPs to efficiently degrade PG poses an exceptional danger to cells. Indeed, purified ShyA almost completely digests purified PG sacculi in vitro (23) through its D,D-endopeptidase activity (42), and the EPs play a crucial role in cell wall degradation as a downstream consequence of exposure to β-lactam antibiotics (27, 30). Interestingly, we found that overproduction of *V. cholerae*'s two principal LysM/M23 EPs did not cause any obvious adverse growth phenotypes (Fig. 1*A*). Functional expression of both EPs was verified either by western blot (ShyA only) (*SI Appendix*, Fig. S1*A*) or via the ability to complement an EP depletion mutant (ShyA and ShyC) (42). Thus, EP-mediated PG cleavage activity is either tightly regulated in vivo or always outpaced by a highly effective cell wall synthesis machinery. However, we also noticed during depletion experiments of isopropyl-β-D-thiogalactopyranoside (IPTG)-inducible ShyA in a background deleted in all other M23 and P60 family EPs (Δ6 endo; i.e., Δ*shyABC*Δ*vc1537*Δ*tagE1,2* P_{IPTG}:*shyA*) that viability declined and morphological defects (compared with a control culture that contained inducer) materialized rapidly (within 1 h) on subculturing into medium without inducer (Fig. 1 *B* and *C*). Western blot analysis revealed that at these early time points ShyA protein levels were still clearly detectable (Fig. 1*D*). Based on these results, we speculated that ShyA might be produced in a predominantly inactive form in vivo. We also estimated native ShyA levels using semiquantitative western blot with purified protein of known concentration as a calibration standard. We estimate that, under exponential growth conditions in rich medium, ShyA is present at a level of ∼1,500 molecules per cell (*SI Appendix*, Fig. S1*B*).

The ShyA Crystal Structure Reveals a Putative Switch from an Inactive to an Active Conformation. Since our genetic data hinted toward the existence of an inactive form of ShyA in vivo, we used a structural approach to probe the mechanistic reason for ShyA putative inactivity. We purified and crystallized two constructs, an N-terminally tagged version (replacing the native signal sequence with a 6xHis-tag) and one tagged at its C terminus (likewise with a deleted signal sequence). These two constructs serendipitously yielded two different structures as detailed below.

Structure of ShyA^{CLOSED}. The tertiary structure of ShyA obtained from the monoclinic crystals grown from the N-terminal His-tagged protein was solved by molecular replacement using the previously determined ShyB structure [Protein Data Bank (PDB) ID code 2GUI (46)] to a resolution of 2.11 Å with good crystallographic statistics (Table 1). The solved structure revealed three domains common in other M23 family EPs (46–48) (Fig. 2*A*). Domain 1 contains an LysM PG binding domain (49). Domain 2 appears to serve as a hinge domain between Domain 1 and Domain 3 and further engages in interactions with a C-terminal α-helix. Finally, Domain 3 contains the M23 domain responsible for cleavage of the peptide bond cross-link (D-Ala–diaminopimelic acid [DAP]) in PG. Domain 1 and Domain 3 have both hydrophobic and electrostatic interactions bringing the two domains into close proximity. We will henceforth refer to this structure as ShyA^{CLOSED} (Fig. 2*B*).

At the interface of the LysM and M23 domains, Domain 1 is predominantly negatively charged, and Domain 3 is positively charged. At the center of the interface are van der Waals interactions between L109 and L344 in Domain 1 and 3, respectively. Additionally, the carboxyl group of D112 hydrogen bonds with the hydroxyl group of Y330. Furthermore, Domain 1 residue E103 forms an electrostatic interaction with R371 present on the loop adjacent to the M23 catalytic groove. This combination of electrostatic and van der Waals interactions presumably serves to enhance interaction between the two domains and further appears to occlude the catalytic groove of the M23 domain. At the end of Domain 3, the ShyA polypeptide forms an amphipathic C-terminal α-helix where hydrophobic residues pack against the β-sheet of Domain 2 and hydrophilic residues are solvent-exposed. A similar helix is also found in Domain 3 of *Neisseria* structures for the EP NGO_1686 (PDB ID codes 6MUK and 3SLU) (47) but not observed in the ShyB crystal structure because the protein construct did not include residues at the C terminus. The presence of this helix in multiple structures may indicate a role in the orientation of Domain 2. The active site residues of ShyA's M23 domain are similar to other M23 EPs, in particular to ShyB and NGO1686 (46, 47). The catalytic Zn^{2+} ion is ligated directly by H297, D301, and H378 and through water molecules to H376 and H345 (Fig. 2*E*). Most of these residues are positioned on an antiparallel beta sheet in Domain 3. However, residue H297 is on an extended loop between two antiparallel beta strands.

Structure of ShyA^{OPEN}. Unexpectedly, the tertiary structure of ShyA obtained from the monoclinic crystals grown from the C-terminal His-tagged protein was drastically different from the ShyA^{CLOSED} structure (Fig. 2 *B* and *C*). For reasons outlined below, we will refer to this structure as ShyA^{OPEN}. Although each domain adopts a very similar conformation as the corresponding domain in ShyA^{CLOSED} (Cα rmsd range from 0.6 to 1.0 Å), the molecule is extended such that there are no interactions between individual domains within one molecule except for the C-terminal helix, which still packs against Domain 2 as it does in ShyA^{CLOSED}. Although diffraction data anisotropy resulted in an electron density map significantly less well resolved than ShyA^{CLOSED}, the electron density for the interdomain linkers in ShyA^{OPEN} was clearly resolved in the initial molecular replacement map and subsequent composite, simulated annealing omit maps of the entire structure (*SI Appendix*, Fig. S2 *B* and *C*).

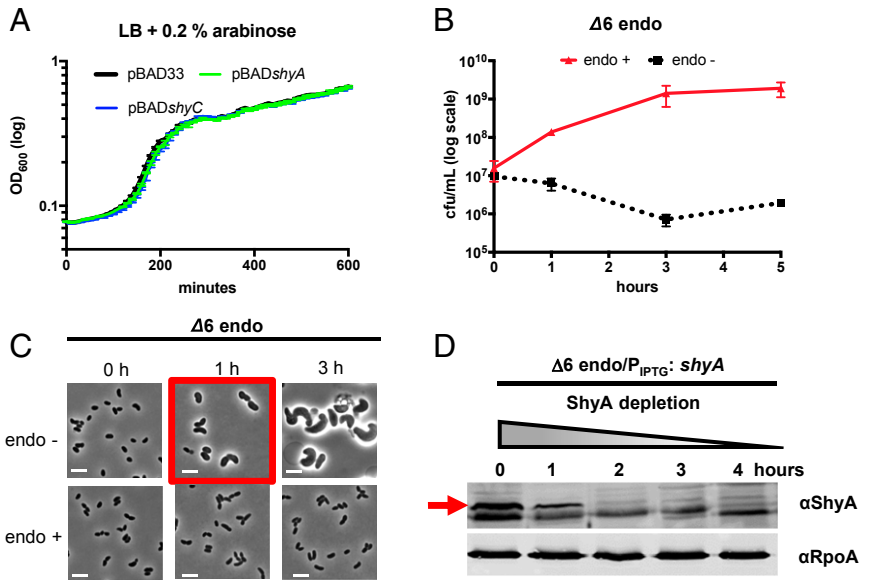

Fig. 1. ShyA overexpression and depletion phenotypes. (*A*) EP overexpression does not affect growth behavior. Strains carrying either empty pBAD or EPs under control of an arabinose-inducible promoter were grown in a Bioscreen growth curve analyzer. (*B* and *C*) Defects associated with EP depletion materialize early in the depletion time course. A Δ6 endo strain (Δ*shyABC* Δ*vc1537* Δ*tagE1/2* P_{IPTG}:*shyA*) was grown overnight in the presence of 200 μM IPTG, washed twice, and resuspended in either the absence ("endo −") or presence ("endo +") of inducer. At designated time points, cells were then either plated on LB agar containing IPTG (*B*) or imaged on an agarose pad (*C*). (Scale bar, 5 μm.) Data in *B* are averages of three independent experiments; error bars represent SD. (*D*) Western blot analysis of in vivo ShyA levels during early depletion time points. The Δ6 endo strain (P_{IPTG}:*shyA*) was treated as described under *B*. At designated time points, ShyA was visualized via western blot using anti-ShyA primary antibody. cfu, colony forming units.

Because the interdomain linkages are likely flexible, an open form in solution could adopt many conformations and not only the overall shape observed in the crystal.

In order to transition between closed and open forms, the ShyA molecule must undergo a 138° rotation of Domain 2 around an axis passing through the Domain 2–Domain 3 linker (near residue 265) (Fig. 2*D*). Most of the changes occur in the interdomain linkages. Because of the rotation of Domain 2, the linker between Domain 3 and the C-terminal helix (~396 to 400) also must change significantly (*SI Appendix*, Fig. S2*C*). The major consequence of the observed conformational change is that Domain 1 has moved significantly away from Domain 3, making the presumed substrate binding site in Domain 3 completely solvent-accessible.

We hypothesized how a minimal model of the D-Ala–DAP dipeptide cross-link (a part of the natural substrate for EPs) containing the scissile bond might be positioned in the putative substrate binding region of $ShyA^{OPEN}$ (*SI Appendix*, Fig. S2*D*). Although not shown in *SI Appendix*, Fig. S2*D*, the scissile amide bond carbonyl points toward the catalytic Zn^{2+} [as proposed for the catalytic mechanism of the M23 peptidase LytM with transition-state analog (50)]. In $ShyA^{CLOSED}$, Domain 1 completely obscures the binding site region to the "right" of the Zn^{2+} atom when viewed in the orientation of *SI Appendix*, Fig. S2*E*. This modeling approach allowed us to test predictions about catalytic residues that are expected requirements for EP function. We created mutations in such residues and tested the resulting mutant protein's activity by its ability to complement (or not) growth of a Δ6 endo strain. Specifically, we tested H345 (predicted to ligate the catalytic water), H297 (coordination of the catalytic zinc), R286, and D301 (predicted to be important based on its proximity to the active site zinc) (Fig. 2*E*). Consistent with important roles in zinc and water coordination, mutating R286, H297, or H345 to an alanine completely abrogated ShyA activity in vivo (Fig. 2*F*), while expression levels for these mutants were not affected (*SI Appendix*, Fig. S1*C*). We had previously found that an H376A mutation rendered the protein nonfunctional as well (23), also consistent with its role in hydrogen bonding to the Zn-bound catalytic water molecule. Thus, consistent with our structural prediction, residues D301, H345, H378, R286, H297, and H376 are crucial for ShyA's EP function and thus, serve to functionally validate our structure's in vivo significance.

In summary, our structural data suggest that ShyA likely assumes two conformations in equilibrium. The closed form is inactive, and only the open form is predicted to be active due to PG substrate accessibility. We hypothesize that the in vitro activity that we observe with purified ShyA is the result of conformational switching of a subfraction of ShyA molecules in solution. Indeed, we previously noticed that the C-terminally tagged construct that yielded the open conformation was highly active on its PG substrate (reaction times 30 min to 3 h) (23), while the N-terminally tagged construct (as well as untagged ShyA) required much longer reaction times of 12 to 16 h (42) to complete PG digestion.

Mutations Predicted to Favor the Open Conformation Increase ShyA Toxicity In Vivo. Based on our structural predictions that allowed us to assign a putative inhibitory role for Domain 1, we created mutations that we expected to reduce interactions between Domain 1 and Domain 3 (Fig. 3*A*). We started by making targeted domain deletions and assessed their toxicity and function. We first created a truncated protein that lacks Domain 1 (Dom1) altogether by fusing a standard periplasmic signal sequence [of DsbA (51)] with ShyA residues 161 to 430. To control for protein secretion effects, we also constructed a full-length ShyA version that had its native signal sequence (residues 1 to 35) replaced with that of DsbA ($DsbA_{ss}$-ShyA). Overexpressing the $ShyA^{\Delta Dom1}$ construct in a wild-type background yielded no reduction in plating efficiency; however, colonies were generally smaller than the controls (Fig. 3*B*). Upon visualization of cells overexpressing $ShyA^{\Delta Dom1}$, however, we noticed striking morphological defects. Most notably,

Table 1. Data collection and refinement statistics

	ShyA^{CLOSED}, PDB ID code 6UE4	ShyA^{OPEN}, PDB ID code 6U2A
Wavelength (Å)	0.9775	1.078
Space group	$P\,2_1$	$C\,2$
Unit cell a, b, c (Å)	61.12 87.25 74.97	75.27 82.49 82.52
Unit cell α, β, γ (deg)	90 100.37 90	90 102.69 90
Resolution range for data processing (Å)	49.55–2.08 (2.12–2.08)	54.9–2.03 (2.28–2.03)
Resolution cutoffs from anisotropic analysis (Å)		
0.78a^* – 0.63c^*		2.32
b^*		3.02
0.49a^* + 0.87c^*		1.98
Total reflections measured	309,587 (15,147)	121,494 (5,375)
Unique reflections	46,207 (2,295)	17,391 (870)
Multiplicity	6.7 (6.6)	7.0 (6.18)
Completeness (%)		
Spherical		54.1 (9.2)
Ellipsoidal		89.8 (66.7)
Mean I/sigma(I)	12.45 (2.00)	9.8 (1.61)
Wilson B factor	25.4	60.31
R_{merge}	0.119 (0.647)	0.055 (1.13)
R_{meas}	0.129 (0.702)	0.059 (1.23)
R_{pim}	0.049 (0.270)	0.022 (0.487)
Correlation coefficient	Not applicable (0.815)	0.998 (0.549)
Resolution range for refinement (Å)	49.55–2.08 (2.13–2.08)	36.58–2.3 (2.38–2.3)
Reflections used in refinement	43,887 (3,223)	16,347 (665)
Completeness (%)	99.4 (99.3)	74.38 (30.42)
Reflections used for R_{free}	2,297 (156)	842 (45)
R_{work}	0.178 (0.226)	0.253 (0.371)
R_{free}	0.233 (0.276)	0.295 (0.425)
No. of nonhydrogen atoms	5,868	2,878
Macromolecules	5,747	2,867
Ligands	8	1
Solvent	113	10
Protein residues	705	360
rms (bonds)	0.014	0.003
rms (angles)	2.007	0.57
Ramachandran favored (%)	98.0	96.1
Ramachandran allowed (%)	2.0	3.9
Ramachandran outliers (%)	0.00	0.00
Rotamer outliers (%)	2.00	0.00
Clash score	5.0	5.40
Average B factor	27.6	77.4
Macromolecules	27	77.5
Ligands	33.6	79.8
Solvent	30.5	55.9

Statistics for the highest-resolution shell are shown in parentheses. deg, degree.

we observed a high degree of sphere formation, indicative of increased PG cleavage activity (Fig. 3*C*). Overexpression of wild-type ShyA, an active site mutant (ShyA^{H376A}), DsbA$_{ss}$-ShyA, or a Domain 1 + Domain 2 truncation (residues 266 to 430) did not cause any growth or morphological defects (Fig. 3 *B* and *C*). Thus, Domain 1 plays an important role in suppressing ShyA overexpression toxicity, consistent with a role in active site inhibition.

We next focused our attention on the hydrophobic interactions between L109 and L344, the salt bridges between D112/Y330 and E103/R371, and the general acidic–basic interaction of the entire domain interface (Fig. 3*A*) to create additional mutants that might favor an open conformation. We predicted that mutating L109 to a basic residue would strongly repel the basic patch in Domain 3 and also sterically clash with L344 in Domain 3, opening the structure. Remarkably and consistent with this hypothesis, overexpression of the ShyA^{L109K} mutant caused a near 100,000-fold plating defect and resulted in population-wide sphere formation when expressed in liquid medium (Fig. 3 *B* and *C*). To further probe the L109–L344 interaction's involvement in Domain 1 to 3 interactions, we reasoned that a negative charge addition in the opposing L344 residue would electrostatically interact with the K109 residue to promote the closed conformation and reduce ShyA^{L109K} toxicity. Consistent with a functional interaction between L109 and L344, mutating L344 to an aspartic acid (L344D) in the L109K background restored wild-type growth on a plate and normal morphology (Fig. 3 *B* and *C*); importantly, ShyA^{L109KL344D} was expressed at similar levels as wild-type ShyA and ShyA^{L109K} (*SI Appendix*, Fig. S1).

We next turned to the predicted salt bridge between E103 and R371. To potentially interrupt this interaction and consequently destabilize Domain 1–Domain 3 interactions, we introduced an alanine substitution in E103. The resulting ShyA^{E103A} mutant caused loss of rod shape and sphere formation, yet no plating

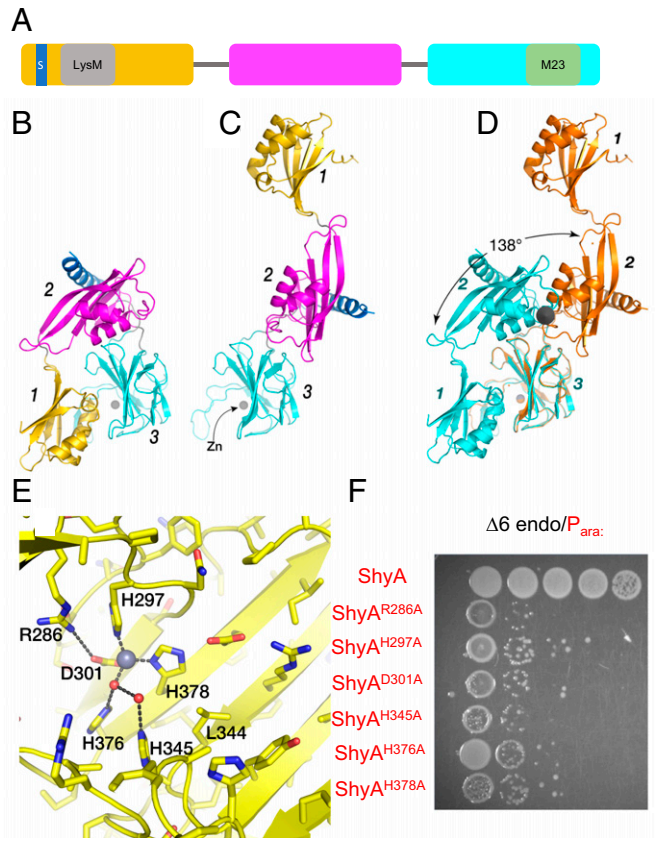

Fig. 2. Comparison of the two observed conformations of ShyA. (*A*) Diagram of predicted ShyA domains. The signal sequence (S), LysM domain, and M23 catalytic domain are indicated. (*B*) Cartoon diagram of ShyA^{CLOSED} (PDB ID code 6UE4) determined from crystals grown from protein containing an amino-terminal 6xHis-tag. Each domain is numbered and highlighted in a different color. (*C*) Cartoon diagram of ShyA^{OPEN} (PDB ID code 6U2A) from crystals grown from ShyA protein containing a carboxyl-terminal 6xHis-tag. Domain 3 is oriented exactly like Domain 3 in *B*. (*D*) Domain 3 of each structure is superposed. Closed form is in cyan, and open form is in orange. The gray solid circle is an end-on view of the 138° rotation axis that relates Domain 2 of the two different structures. Note that the C-terminal helix packing against Domain 2 is also related by this same transformation. (*E*) Close-up view of the predicted ShyA active site showing residues putatively required for catalytic function. Red spheres represent water molecules; the gray sphere represents the catalytic zinc atom. (*F*) Validation of predicted active site residues in a Δ6 endo background (Δ*shyABC* Δ*vc1537* Δ*tagE1/2* P_{IPTG}:*shyA*) where ShyA is under IPTG control. The indicated mutants under control of an arabinose-inducible promoter were plated in the absence of IPTG but in the presence of arabinose to test for functionality of variants when expressed as the sole EP.

defect, similar to the ΔDomain 1 mutant (Fig. 3*C*). Western blot analysis revealed that L109K and E103A were expressed at levels similar to wild-type ShyA (*SI Appendix*, Fig. S1), suggesting that mutant toxicity was not simply the result of enhanced protein accumulation. Lastly, we also tested mutations in D112 (creating ShyA^{D112E} and ShyA^{D112A}). D112 is predicted to hydrogen bond with Y330 in Domain 3. Again, consistent with disruption of this stabilizing interaction, both ShyA^{D112E} and ShyA^{D112A} caused morphological defects upon overexpression as well as a mild plating defect (small colonies) (*SI Appendix*, Fig. S3). Taking all in vivo results together, we conclude that mutations that are expected to disrupt interactions between Domains 1 and 3 activate the protein to varying degrees.

Mutations Predicted to Favor the Open Conformation Increase ShyA Activity In Vitro. While predicted open conformation mutants exhibited higher toxicity in vivo, we sought to confirm that this was indeed due to higher PG cleavage activity. We purified N-terminally tagged ShyA$^{67-426}$ as well as its derivatives ShyA^{L109K} and ShyA$^{L109K/L344D}$ and measured their activity by assaying digestions of purified whole PG sacculi. With ShyA$^{67-426}$, we observed slow digestion proceeding to completion after 20 h, but comparatively little activity after short (10-min to 3-h) incubation periods (Fig. 4*A* and *SI Appendix*, Fig. S4). Thus, this version of ShyA (retaining domains in the ShyA^{CLOSED} structure) is active at a low level. In contrast, the ShyA^{L109K} derivative of this construct almost completely digested purified sacculi within 10 min with no further activity after 20 h of incubation (Fig. 4*B*). Thus, the L109K mutation enhances PG cleavage activity in vitro. ShyA$^{L109K/L344D}$ exhibited significantly reduced activity compared with ShyA^{L109K} at the earliest time point (Fig. 4 *B* and *C*), although activity was still considerably higher than that of wild-type ShyA and remained at ShyA^{L109K} levels for the remainder of the time course. Thus, establishing an ionic bridge between Domains 1 and 3, while drastically reducing toxicity in vivo, still results in a considerably faster reaction rate than the wild-type protein. We speculate that the difference between in vivo and in vitro results reflects that the geometry of the engineered ionic bridge is not ideal, and the two residues may still sterically clash in vitro. The specific periplasmic environment might reduce the conformational consequences of this steric clash: for example, through molecular crowding, a condition not readily reproducible in vitro. Another observation lent support to the idea that the ShyA$^{L109K/L344D}$ has reduced activity in vivo; we found that this variant only partially complemented a Δ6 endo strain (*SI Appendix*, Fig. S5). However, both in vitro and in vivo, the L344D mutation reduced activity of ShyA^{L109K}, providing additional evidence that enhancing Domain 1–Domain 3 interactions renders ShyA less active than reducing such interactions.

To obtain information about the ShyA conformation in solution, we purified ShyA (67 to 426) and its mutant variants without epitope tags and measured small-angle X-ray scattering (SAXS) profiles (*SI Appendix*, Fig. S6 *A* and *B*). These revealed a significant increase in the radius of gyration (R_g) between wild-type ShyA (R_g = 23.6 ± 0.1 Å, D_{max} = 75 Å) and the L109K mutant (R_g = 28.8 ± 0.3 Å, D_{max} = 105 Å) protein (*SI Appendix*, Fig. S6 *C* and *D* and Table S3). The first R_g value was consistent with the theoretical R_g predicted from the ShyA^{CLOSED} crystal structure (23.4 Å). The L109K R_g suggested a more open mutant structure but not as open as the ShyA^{OPEN} structure (predicted R_g of 32.6 Å). We modeled a partially open conformation of the L109K mutant by rotating Domains 1 and 2 of the ShyA^{OPEN} structure 90° about the axis previously determined from the Domain 2 superpositions (Fig. 2*D*). This model (denoted ShyA^{PARTIAL}) had a predicted R_g of 29.2 Å, in close agreement with that observed experimentally for the L109K mutant. We then calculated three-dimensional electron density maps from the one-dimensional SAXS data with DENSS (52). As shown in Fig. 4*D*, the ShyA^{CLOSED} and the partially open model fit nicely into their respective contoured densities.

We speculated that ShyA^{PARTIAL} could be quite dynamic in solution and that multiple ShyA conformations might give better fits to the L109K SAXS data. Fits to each of the three models were poor (*SI Appendix*, Fig. S6 *C–E*), but an ensemble of three conformations (24.8% ShyA^{CLOSED}, 8.7% ShyA^{OPEN}, and 66.1% ShyA^{PARTIAL}) gave the best fit to the L109K SAXS data (χ^2 = 0.87), much better than ShyA^{PARTIAL} alone (χ^2 ~ 58.1) (*SI Appendix*, Fig. S6*F* and Table S3). Thus, the solution structure of L109K is sampling multiple conformations but exists mostly in the partially open conformation.

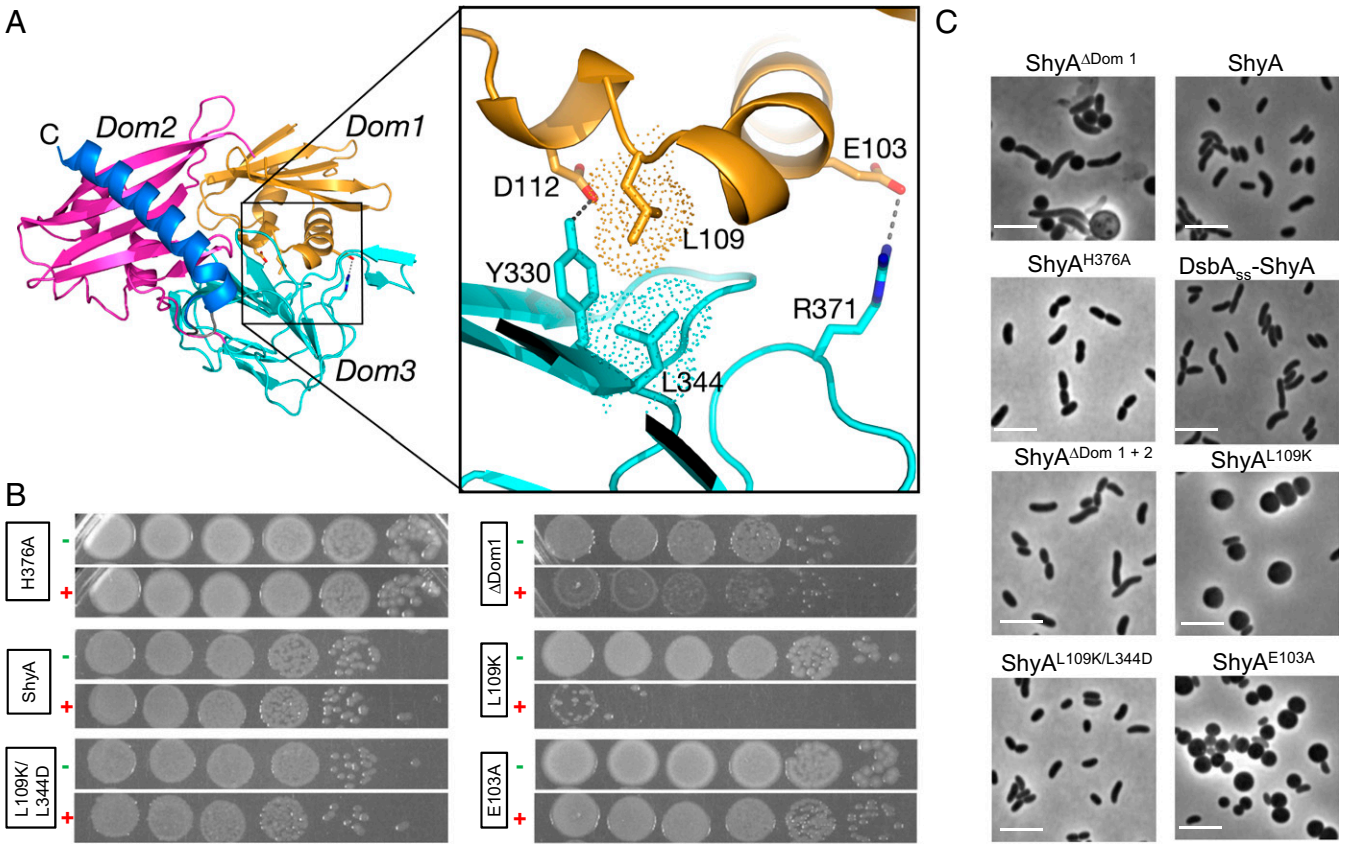

Fig. 3. ShyA activity is enhanced by mutating Domain 1–Domain 3 interface residues. (*A*) Overall domain structure of ShyA with zoomed-in view of residues predicted to mediate Domain 1–Domain 3 interactions (*Inset*). Domain colors are as in Fig. 2 *B–D*. (*B*) Wild-type *V. cholerae* carrying the indicated mutant construct (arabinose inducible) was diluted and spot plated on plates containing either no inducer (–) or 0.2% arabinose (+). (*C*) Wild-type *V. cholerae* carrying the indicated plasmid construct was grown to exponential phase (OD_{600} ~ 0.4) in LB/Cm (20 μg/mL) and induced for 3 h with 0.2% arabinose followed by imaging on an agarose pad. (Scale bar, 5 μm.)

Conformational Regulation May Be Widespread among Divergent M23 Endopeptidases. We asked whether M23 EPs from other bacteria might exhibit a mode of regulation similar to the one that we are proposing for ShyA. Indeed, published structures of EPs from divergent pathogens, namely Csd3 (*Helicobacter pylori*) and NGO1686 (*Neisseria gonorrheae*), appeared to assume a domain organization remarkably similar to that of ShyA (Fig. 5*A*) (47, 48). In addition, a homology model was created for MepM (*E. coli*) using the $ShyA^{CLOSED}$ structure. We created mutations in NGO_1686 of *N. gonorrheae* and MepM of *E. coli* to test predictions about enzyme activation. For NGO_1686, we identified a residue (E132) that we implicated in interdomain connections (via a salt bridge between E132 and R293) (*SI Appendix*, Fig. S7) and tested a mutation (E132R) that we predicted to destabilize this interaction, analogous to E103A in ShyA. The MepM model does not have a clearly identifiable acidic–basic Domain 1–Domain 3 interface, and we thus simply created a ΔDomain 1 variant that should relieve catalytic inhibition by Domain 1.

We expressed NGO1686 and its $NGO1686^{E132R}$ variant heterologously in *E. coli*. While neither the mutant variant nor the wild-type protein caused a strong plating defect upon induction (although colonies were smaller for the mutant form) (Fig. 5*B*), expression of $NGO1686^{E132R}$ caused a dramatic morphological defect, including sphere formation (Fig. 5*C*). A slight defect was visible even in the wild-type protein, but this was exacerbated in the mutant. To assess enhanced NGO1686 toxicity more quantitatively, we also performed a mecillinam/moenomycin sensitivity assay. In *E. coli*, increased EP activity imparts mecillinam resistance, likely due to overactivation of aPBPs (54). We predicted that such aPBP overactivation should also render these cells more susceptible to moenomycin, an aPBP inhibitor (55). We thus performed a Kirby–Bauer zone of inhibition assay (56) on *E. coli* overexpressing an inactive version of ShyA ($ShyA^{H376A}$, negative control), NGO1686, or its $NGO1686^{E132R}$ derivative. Overexpression of $NGO1686^{E132R}$, but not the wild-type protein or inactive $ShyA^{H376A}$, increased resistance against mecillinam, again suggesting that indeed the E132R mutation enhances NGO1686 activity. The $NGO1686^{E132R}$ also increased sensitivity to moenomycin (Fig. 5*D*), which may either likewise reflect an increased reliance on aPBPs (consistent with increased EP activity according to the model in ref. 54) or an outer membrane permeability defect induced under these cell wall damaging conditions.

Overexpressing $DsbA_{ss}$-$MepM^{\Delta Domain1}$ in its native host *E. coli* dramatically reduced plating efficiency compared with the wild-type version of the protein (*SI Appendix*, Fig. S8). Interestingly, $DsbA_{ss}$-MepM (the true parental to $MepM^{\Delta Domain1}$) exhibited slightly enhanced toxicity (manifesting as small colonies) compared with the wild-type protein, suggesting that soluble MepM by itself is more active than its predicted membrane-bound form. In cumulation, we demonstrate that ShyA's domain organization is conserved across divergent gram-negative pathogens and suggest that the inhibitory role of Domain 1 constitutes a widespread mechanism of regulation.

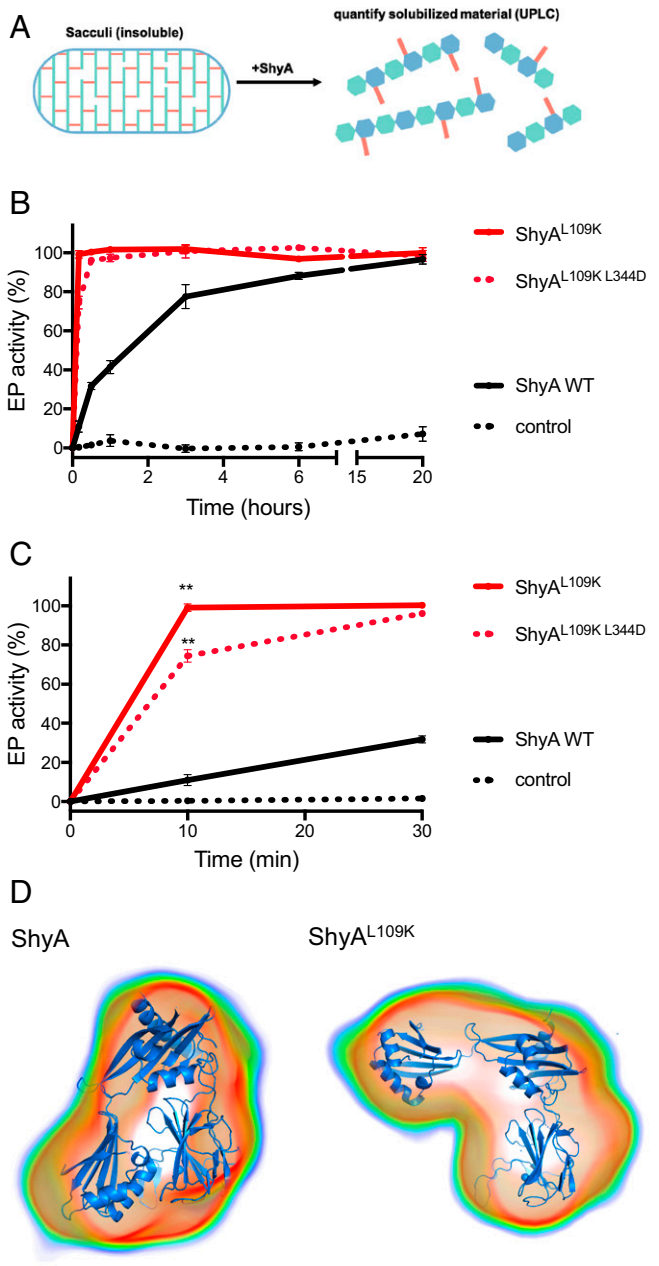

Fig. 4. In vitro toxicity of hyperactive ShyA variants. (*A*) Overview of reaction. Purified (insoluble) PG sacculi are digested with ShyA, and the solubilized material is quantified via ultra-performance liquid chromatography (UPLC). (*B*) Purified (N-terminally His-tagged) ShyA and its derivatives were mixed with purified PG sacculi and incubated at 37 °C. At the indicated time points, samples were withdrawn, and reactions were stopped by boiling and digested with muramidase followed by analysis on UPLC. EP cleavage activity was calculated as area under the curve of both solubilized PG material and remaining pellet (*Materials and Methods* has details). Data are averages of three independent reactions; error bars represent SD. (*C*) Enhanced (first 30-min reaction time) view of the graph in *B* to illustrate significant difference between ShyA^{L109K} and ShyA$^{L109K/L344D}$. The control is purified PG without addition of EPs. **Statistical significance (*t* test, $P < 0.001$). (*D*) ShyA^{CLOSED} and a partially open model docked into electron density maps calculated by DENSS (52) from the one-dimensional SAXS scattering curves measured from ShyA wild-type (*Left*) and ShyA^{L109K} (*Right*), respectively. Volume is colored from blue to red in three dimensions. Red density represents 4σ above the map mean. Front surface has been removed by the front clipping plane, while white regions are due to back clipping plane cutting into density. WT, wild type.

Discussion

The mechanism of regulation of EPs during cell elongation is poorly understood for gram-negative bacteria. Data from *E. coli* and *Pseudomonas aeruginosa* point toward proteolytic turnover (44, 45); however, in *E. coli* this mechanism of regulation appears to be more dominant during stationary-phase remodeling, and its role in *P. aeruginosa* is unclear. Notably, deleting EP-specific proteases only causes minor phenotypes under laboratory growth conditions and does not seem to affect cell elongation in exponential phase unless severe osmotic conditions are applied (44, 45). Here, we present data suggesting a conformational switch mechanism of activation for LysM/M23 EPs to effectively regulate cell wall remodeling during cellular expansion. Interestingly, ShyA mutants that we predicted to favor active conformations differed in the severity of their toxicity. For example, only the L109K mutation caused a strong plating defect upon induction. The ΔDomain1, E103A, and D112E mutations caused sphere formation similar to the L109K mutation; however, these former mutants were able to ultimately form colonies on a plate. The open conformation observed in the crystal structure likely represents an extreme (possibly induced by high protein concentrations that promoted intermolecular Domain 1–Domain 3 interactions, stabilizing the wide-open conformation), while the situation in vivo (as indicated by our SAXS analysis) is likely more dynamic, with various degrees of opening up of the ShyA^{CLOSED} structure. It is possible that the L109K change simply results in the strongest repellent effect between Domain 1 and Domain 3, while E103A/D112E present as more dynamic forms with an open–closed equilibrium that is just pushed slightly toward the open state.

Our data raise the possibility that bacteria maintain a large pool of inactive EP precursors that are actuated only when or where needed. In line with this thinking, conformational switch regulation appears to be the preferred mode of regulation for other cell wall-active enzymes as well (57–60). This strategy as opposed to transcriptional regulation would allow for quick responses to environmental conditions that may require enhanced cleavage activity. A large inactive pool of EPs would also explain an apparent oddity. A modeling approach has suggested that less than 100 "dislocation events" (i.e., PG cleavage events) per cell are sufficient for growth (61), and previous biochemical work demonstrated that a similarly low number of cell wall synthesis complexes is active per generation (62). Compared with these estimates, EP numbers have been determined to be much higher using ribosome profiling in the model organism *E. coli* [between ∼300 (MepM) and ∼4,000 (spr) (63)]. While effective Spr levels are likely much lower in vivo due to the activity of the periplasmic protease Prc (45), it is still reasonable to assume that this number might be higher than 100. Our estimate for the number of ShyA molecules per cell (∼1,500) appears to be within the range of other EPs. Thus, the number of EP molecules in the cell potentially exceeds the number of active molecules theoretically required to sustain growth. It is tempting to speculate that these surplus molecules indeed provide a reservoir for changing growth conditions.

While we have not identified the signal promoting this conformational switch, we hypothesize that this might be an interaction with cell wall synthases or the protein complexes that they are embedded in to enable tight coordination between synthesis and degradation. Importantly, however, the aPBPs themselves are not likely activators of conformational switching—data in *E. coli* conversely suggest that EPs promote aPBP activity (54), while aPBP abundance does not appear to be limiting for EP activity. In *E. coli*, the lipoprotein NlpI was recently identified as a multifunctional regulator of EP activity and coordinator of hydrolysis with PG synthesis functions (40). NlpI was shown to inhibit the activity of the ShyA homolog MepM, and its

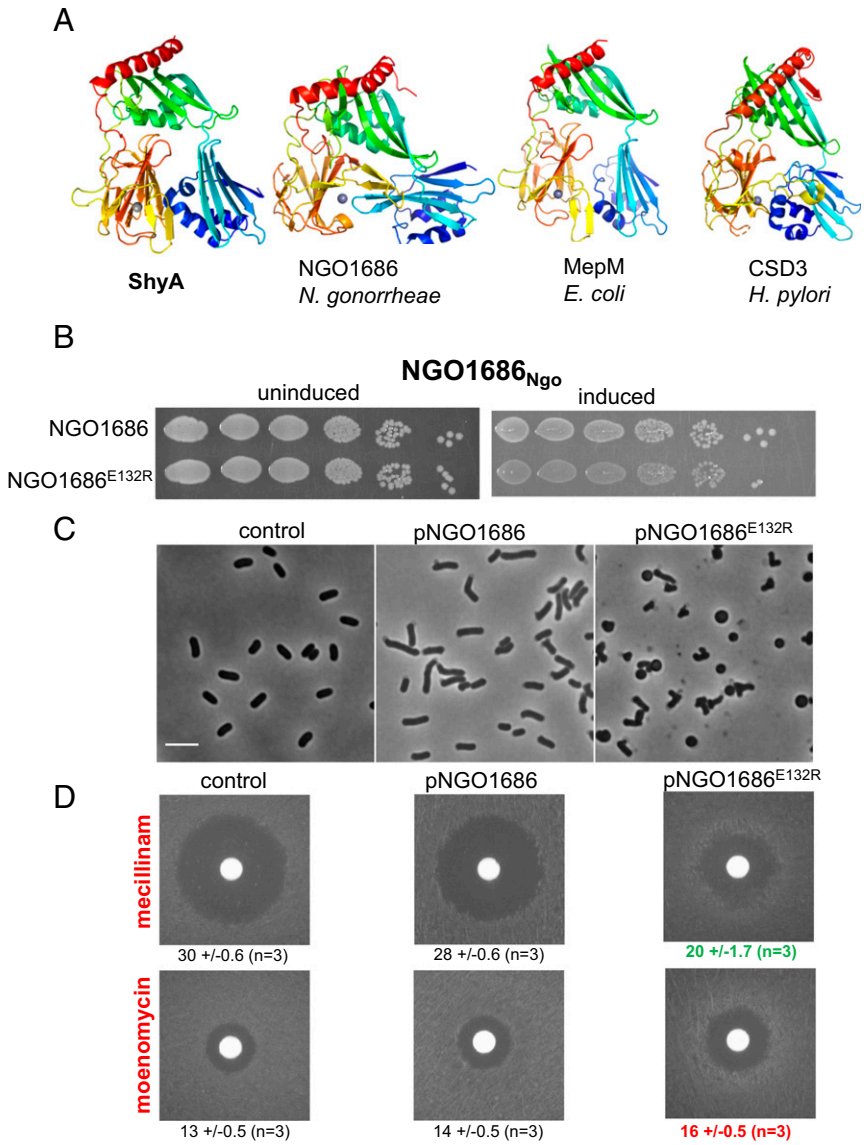

Fig. 5. ShyA functional domain organization is conserved in divergent gram-negative pathogens. (*A*) Domain organization of LysM/M23 EPs. Structures were either obtained from published sources (CSD3 and NGO_1686; PDB ID codes 4RNY and 6MUK, respectively) or modeled onto our ShyA structure using the Swiss Model server (53) (MepM). Polypeptides are rainbow colored from blue at the N terminus to red at the C terminus. (*B*) Overexpression toxicity of NGO1686^{E132R}. Strains carrying arabinose-inducible EPs were plated in the absence (uninduced) or presence (induced) of 0.2% arabinose. (*C*) MG1655 carrying pBAD33 or its derivatives containing wild-type NGO_1686 or NGO1686^{E132R} were grown to midexponential phase (OD_{600} ~ 0.4) and induced with 0.2% arabinose followed by imaging on agarose pads. (Scale bar, 5 μm.) (*D*) MG1655 carrying the indicated plasmids was plated evenly (~10^8 colony forming units [cfu]) on LB agar containing 0.2% arabinose and Cm (20 μg/mL). A filter disk containing mecillinam (10 μL of 20 mg/mL stock) or moenomycin (10 μL of 5 mg/mL stock) was then placed in the center of the plate followed by incubation for 24 h at 37 °C. Numbers below the images indicate zone of inhibition in millimeters ± SD. Control, ShyA^{H376A}; Ngo, *N. gonorrheae*.

V. cholerae homolog is thus likely not the ShyA activator. However, it is possible that similar protein–protein interactions may induce the observed conformational switch in EPs, analogous to activation of amidases by their EP-like regulators (14, 29, 64). Alternatively, EPs might recognize intrinsic substrate cues in PG (e.g., tension state), in line with Arthur Koch's "smart autolysin" hypothesis (65). ShyA possesses an LysM carbohydrate binding domain (49) in Domain 1, and in the smart autolysin scenario, an interaction of this domain with PG might enhance the switch to an active form under specific (e.g., osmotic challenge) conditions. From a broader perspective, our data add to the emerging theme of a multifaceted regulatory system for EPs (transcriptional regulation, posttranslational degradation, conformational change). This complex system likely reflects the necessity of tightly controlling cell wall degradation during cell elongation in rapidly changing environments.

Materials and Methods

All strains and reagents will be available on reasonable request to the corresponding author. All protein structural data have been deposited in the PDB (https://www.rcsb.org [PDB ID codes 6UE4 and 6U2A]).

Media, Chemicals, and Growth Conditions. Strains were grown in lysogeny broth (LB) medium (Fisher Scientific; catalog no. BP1426-2) at 37 °C and shaken at 200 rpm unless otherwise indicated. Antibiotics were used at the following concentrations: streptomycin (200 μg/mL), chloramphenicol (Cm; 20 μg/mL), and kanamycin (Kan; 50 μg/mL). Inducers were used at 0.2% (arabinose) or 300 μM (IPTG).

Bacterial Strains and Plasmids. Bacterial strains and oligos are summarized in *SI Appendix*, Tables S1 and S2. All *V. cholerae* strains are derivatives of N16961 (66). Subcloning was conducted in *E. coli* SM10 lambda pir. Isothermal assembly [ITA; Gibson Assembly (67)] was used for all cloning procedures.

ShyA and ShyC were cloned into pBADmob [a pBAD33 derivative containing the mobility region from pCVD442 (68)] using primer pairs TDP484/1302 (ShyA) or TDP486/779 (ShyC). Site-directed mutagenesis was performed using the NEB Q5 site-directed mutagenesis kit (NEB; catalog no. E0554S) using mutagenesis primers summarized in *SI Appendix*, Table S2 with pBADmob*shyA* as a template. pBADmob*NGO1686* was constructed by amplifying the *ngo1686* open reading frame from heat-lysed *N. gonorrhea* ATCC 49226 with primers TDP1365/1367 followed by cloning into Sma1-digested pBADmob via ITA. This plasmid was then used as a template for construction of E132R using the NEB Q5 site-directed mutagenesis kit.

Expression and Purification of Recombinant ShyA with N-Terminal His-Tag. After predicting the periplasmic signal sequence of ShyA with SignalP 4.1, the coding region (residues 36 to 430 for t-ShyA or residues 67 to 426 for a shorter truncated s-ShyA) of the ShyA gene was amplified from *V. cholerae* N16961 genomic DNA using mutagenic primers TD-JHS062 and TD-JHS063 (for t-ShyA) and TD-JHS323 and TD-JHS324 (for s-ShyA). The PCR products were digested with NdeI and BamHI and inserted into the pET-15b plasmid (Novagen) digested with the same enzymes. To create ShyA mutant proteins, site-specific mutagenesis primers (L109K and L109K/L344D, designed with the NEBaseChanger mutagenesis tool) were used with the NEB Q5 site-directed mutagenesis kit (New England Biolabs).

For the purification of 6xHis + ShyA proteins, *E. coli* BL21(DE3) (Novagen) was transformed with the resulting recombinant plasmids [pET15bt-ShyA, pET15bs-ShyA, pET15bs-ShyA(L109K), pET15bs-ShyA(L109KL344D)]. An overnight culture from a single colony was used to inoculate 1 L of Luria–Bertani medium. Cells were grown with vigorous shaking (220 rpm) at 37 °C to an optical density at 600 nm (OD_{600}) of 0.5 and were induced with 1 mM (final concentration) IPTG (Gold Bio; catalog no. I2481C25) for 12 h at 30 °C. Harvested cells were resuspended in binding buffer JHS1 (20 mM Tris·HCl [pH 7.9], 0.5 M NaCl, 25 mM imidazole) and lysed by sonication. N-terminally tagged ShyA and its variants proved insoluble, so inclusion bodies were isolated after centrifugation at 21,002 relative centrifugal force (rcf) for 45 min. For resolubilization of insoluble ShyA from inclusion bodies, pellets were resuspended in solubilization buffer JHS4 (20 mM Tris·HCl [pH 7.9], 0.5 M NaCl, 25 mM imidazole, 3 M urea) and incubated overnight on a rotator at 4 °C. Supernatant containing resolubilized ShyA was centrifuged at 21,002 rcf for 45 min and loaded onto a HisPur Cobalt column (Thermo Scientific; catalog no. 89964), which was then washed with 6 vol of solubilization buffer JHS4 followed by 6 vol of washing buffer JHS5 (20 mM Tris·HCl [pH 7.9], 0.5 M NaCl, 50 mM imidazole, 3 M urea). ShyA protein was eluted with 10 vol of elution buffer JHS6 (20 mM Tris·HCl [pH 7.9], 0.5 M NaCl, 3 M urea) containing a linear imidazole gradient from 100 to 500 mM. Fractions containing ShyA protein were pooled and dialyzed against JHS-D1 buffer (20 mM Tris·HCl [pH 7.9], 250 mM NaCl, 10% [vol/vol] glycerol, 2 mM ethylenediaminetetraacetic acid [EDTA], 0.5 M urea) to remove imidazole and cobalt ions; then, they were dialyzed against buffer JHS-D2 (20 mM Tris·HCl [pH 7.9], 150 mM NaCl, 20% glycerol, 0.5 mM $ZnSO_4$) to remove urea and add back zinc and finally, buffer JHS-D3 (20 mM Tris·HCl [pH 7.9], 150 mM NaCl, 30% glycerol).

Crystallization and Structure Solution of ShyA with N-Terminal His6 Tag. The 6xHis + t-ShyA was purified as above, dialyzed in JHS-fast protein liquid chromatography (FPLC) buffer (20 mM Tris·HCl [pH 7.9], 150 mM NaCl), concentrated by centrifugal filter devices (Millipore; 10,000 molecular weight cut-off [MWCO]), and then further purified by FPLC size exclusion chromatography using a HiLoad 16/60 Superdex 200 prep-grade column (GE Healthcare Life Sciences). Pure 6xHis + t-ShyA fractions were collected and concentrated up to 11.4 mg/mL. Protein concentration was measured via ultraviolet absorbance at 280 nm and calculated using ShyA's molar extinction coefficient (ε_{280} = 37,550 M^{-1} cm^{-1}, https://web.expasy.org/protparam/). Protein purity was confirmed by sodium dodecyl sulfate/polyacrylamide gel (SDS/PAGE) with Coomassie blue staining.

For crystallization of ShyA, the concentration of FPLC-purified ShyA was adjusted to 2.7 mg/mL. Concentrated protein was combined with purified PG sacculi [prepared as described previously (23)], and crystallization conditions were screened at room temperature using a Crystal Phoenix liquid handling robot (Art Robbins Instruments). Crystals optimally grew by mixing protein and precipitant (0.2 M malonic acid [pH 6.0], 16% polyethylene glycol [PEG] 3350) and incubating by hanging drop vapor diffusion. Rectangular cuboid crystals formed from these conditions after 3 d at room temperature. Crystals were then transferred to cryoprotectant consisting of precipitant containing 25% (vol/vol) glycerol. Crystals were frozen with a liquid nitrogen stream at Macromolecular Diffraction at Cornell High Energy Synchrotron Source beamline F1 at the Cornell High Energy Synchrotron Source. The diffraction data were indexed and scaled using the HKL2000 software (69). The crystal structure was solved by molecular replacement using the AMoRe Suite (70) package in CCP4 (Collaborative Computational Project) with ShyB (PDB ID code 2GU1) as a search model. The $ShyA^{CLOSED}$ model was built using iterative cycles of model building with COOT software (71) and Refmac5 (72) for refinement. Data and refinement statistics are shown in Table 1. $ShyA^{CLOSED}$ was deposited in the PDB under ID code 6UE4.

Purification, Crystallization, and Structure Solution of ShyA with C-Terminal His-Tag. Competent *E. coli* Rosetta-gami 2 (DE3; Novagen) cells were transformed with pET28-VcShyA(36-430)-His6 (23) in the presence of Cm (100 μg/mL) and Kan (40 μg/mL). Two 2.8-L Fernbach flasks each containing 450 mL Terrific Broth (Research Products International) were inoculated 1:100 with an overnight culture and grown in the presence of Cm and Kan at 37° with shaking. When the cultures reached an OD (at 600 nm) of 1.0 (~7 h), flasks were transferred to a precooled 22 °C incubator for 1 h before inducing each with 0.4 mM IPTG and shaking for another 17 h at 22 °C. After centrifugation, the cell pellet from each flask was suspended in 30 mL lysis buffer (300 mM NaCl, 20 mM Na phosphate [pH 7.5]) containing one-half of a Roche cOmplete Protease Inhibitor Mixture (EDTA-free) tablet and frozen at −80 °C.

After thawing the cell suspension from one flask, the other half of the protease inhibitor tablet was added to the suspension along with 5 μg/mL DNase I. The suspension was passed three times through an Emulsiflex-C3 homogenizer at 4 °C (air pressure ~20,000 pounds per square inch) and then centrifuged in a Sorvall SS-34 rotor at 20,000 rpm (48,000 × *g*) for 30 min. Finally, the lysate was filtered through a 0.45-μm filter.

A 6.5-mL Tricorn column (GE Healthcare) was packed with HisPur Cobalt Resin (Thermo Fisher) and preequilibrated with buffer A (300 mM NaCl, 50 mM Tris·HCl [pH 7.5]). The lysate was loaded onto the column at 1 mL/min, washed at 2 mL/min with buffer A, and then washed with 2 and 4% buffer B (300 mM NaCl, 300 mM imidazole, 50 mM Tris·HCl [pH 7.5]) until absorbance at 280 nm reached baseline. The column was eluted with 60% buffer B until A_{280} reached baseline. Protein was concentrated to 20 mg/mL, and 10% (vol/vol) glycerol was added. Aliquots of 0.5 mL were frozen in liquid nitrogen and stored at −80 °C.

Before setup of crystallization experiments, a frozen protein aliquot was thawed and loaded onto a Superdex HR 75 10/300 (GE Healthcare) size exclusion column and eluted with 150 mM NaCl and 20 mM Tris·HCl (pH 7.6) at 0.5 mL/min. The protein peak was analyzed with SDS/PAGE, and the purest fractions were pooled and concentrated to 17.5 mg/mL with an Amicon Ultra-4 30K MWCO concentrator (EMD-Millipore). Protein was screened for crystallization with the Qiagen commercial kits PEG Suite and Classics in 96-well Intelli-Plates (Art Robbins). Sitting drops containing 0.5 μL protein and 0.5 μL precipitant were equilibrated against 100 μL precipitant in the reservoir. The crystal chosen for data collection grew in precipitant containing 0.25 M sodium citrate, 10% polyethylene glycol 3350, and 0.1 M Tris·HCl (pH 6.0). Crystals were transferred to a cryosolvent consisting of 10% (wt/vol) ethylene glycol in the precipitant and frozen in liquid nitrogen.

Diffraction data from monoclinic crystals obtained with protein containing the C-terminal His6-tag were measured at the Life Science Collaborative Access Team (LS-CAT) beamline 21-ID-D, Advanced Photon Source at Argonne National Laboratory, equipped with a Dectris Eiger 9M detector running in continuous mode. Eighteen hundred images, 0.2° oscillation angle each, were processed with autoPROC (Global Phasing Limited) (73). Data collection statistics are summarized in Table 1. Due to significant anisotropy in diffraction limits, an ellipsoidal region of reciprocal surface was calculated by STARANISO in autoPROC and used as a cutoff. Only reflections within this ellipsoid were used for the structure refinement. Anisotropic Debye–Waller corrections were also applied.

Molecular replacement calculations with Phaser (74) failed to produce a solution when either ShyB [PDB ID code 2GU1 (46); 50% sequence identity to ShyA] or the $ShyA^{CLOSED}$ structure was used as a search model. Only after dividing the latter model into individual domains as search models was a significant solution obtained with a log likelihood gain of 1,840 and translation function *Z* score of 41.5. The electron density map was interpretable with the aid of the individual domain structures from the $ShyA^{CLOSED}$ model. Interdomain linkers were clearly resolved confirming the unique structure observed (*SI Appendix*, Fig. S2). Electron density for the C-terminal α-helix could be interpreted with the help of the $ShyA^{CLOSED}$ structure. The model was built with Coot (71) and refined with Phenix (75) with data to 2.3-Å

resolution to an R_{work}/R_{free} of 0.25/0.29 with excellent geometry. The structure, referred to here as ShyA^{OPEN}, was deposited in the PDB as ID code 6U2A with diffraction data archived at https://proteindiffraction.org/ with file name 6U2A.tar.bz2.

ACKNOWLEDGMENTS. We thank David Erickson (Cornell University) for providing us with *N. gonorrhea*. Research in the laboratory of T.D. is supported by NIH Grants R01AI143704 and R01GM130971. Research in the laboratory of M.A.S. was funded by NIH Grant R01GM130971 and the Department of Biological Chemistry, University of Michigan. Research in the laboratory of F.C. is supported by Molecular Infection Medicine Sweden, the Knut and Alice Wallenberg Foundation, the Swedish Research Council, and the Kempe Foundation. Work in the laboratory of Y.M. was supported by NIH Grant 5R01GM116964. This work is partially based on research conducted at the Cornell High Energy Synchrotron Source, which is supported by NSF Award DMR-1829070 and the NIH/National Institute of General Medical Sciences, using the Macromolecular Diffraction at Cornell High Energy Synchrotron Source facility, which is supported by NIH Award GM-124166 through its National Institute of General Medical Sciences. This research used resources of the Advanced Photon Source (APS), a US Department of Energy (DOE) Office of Science User Facility operated for the DOE Office of Science by Argonne National Laboratory under Contract DE-AC02-06CH11357. Use of the LS-CAT Sector 21 was supported by the Michigan Economic Development Corporation and the Michigan Technology Tri-Corridor (Grant 085P1000817). The SAXS study used the 12-ID-B beamline of the APS and was supported (in part) by the Intramural Research Program of the NIH, National Cancer Institute (NCI), Center for Cancer Research and funds from the NCI under Contract HHSN26120080001E.

1. T. Schneider, H. G. Sahl, An oldie but a goodie—cell wall biosynthesis as antibiotic target pathway. *Int. J. Med. Microbiol.* **300**, 161–169 (2010).
2. K. Emami *et al*., RodA as the missing glycosyltransferase in *Bacillus subtilis* and antibiotic discovery for the peptidoglycan polymerase pathway. *Nat. Microbiol.* **2**, 16253 (2017).
3. M. Banzhaf *et al*., Cooperativity of peptidoglycan synthases active in bacterial cell elongation. *Mol. Microbiol.* **85**, 179–194 (2012).
4. E. Sauvage, F. Kerff, M. Terrak, J. A. Ayala, P. Charlier, The penicillin-binding proteins: Structure and role in peptidoglycan biosynthesis. *FEMS Microbiol. Rev.* **32**, 234–258 (2008).
5. H. Zhao, V. Patel, J. D. Helmann, T. Dörr, Don't let sleeping dogmas lie: New views of peptidoglycan synthesis and its regulation. *Mol. Microbiol.* **106**, 847–860 (2017).
6. A. Taguchi *et al*., FtsW is a peptidoglycan polymerase that is functional only in complex with its cognate penicillin-binding protein. *Nat. Microbiol.* **4**, 587–594 (2019).
7. A. J. Meeske *et al*., SEDS proteins are a widespread family of bacterial cell wall polymerases. *Nature* **537**, 634–638 (2016).
8. E. R. Rojas *et al*., The outer membrane is an essential load-bearing element in Gram-negative bacteria. *Nature* **559**, 617–621 (2018).
9. J. C. Gumbart, M. Beeby, G. J. Jensen, B. Roux, *Escherichia coli* peptidoglycan structure and mechanics as predicted by atomic-scale simulations. *PLoS Comput. Biol.* **10**, e1003475 (2014).
10. L. T. Nguyen, J. C. Gumbart, M. Beeby, G. J. Jensen, Coarse-grained simulations of bacterial cell wall growth reveal that local coordination alone can be sufficient to maintain rod shape. *Proc. Natl. Acad. Sci. U.S.A.* **112**, E3689–E3698 (2015).
11. L. K. Sycuro *et al*., Peptidoglycan crosslinking relaxation promotes *Helicobacter pylori*'s helical shape and stomach colonization. *Cell* **141**, 822–833 (2010).
12. D. C. Yang, K. M. Blair, N. R. Salama, Staying in shape: The impact of cell shape on bacterial survival in diverse environments. *Microbiol. Mol. Biol. Rev.* **80**, 187–203 (2016).
13. T. Uehara, K. R. Parzych, T. Dinh, T. G. Bernhardt, Daughter cell separation is controlled by cytokinetic ring-activated cell wall hydrolysis. *EMBO J.* **29**, 1412–1422 (2010).
14. N. T. Peters, T. Dinh, T. G. Bernhardt, A fail-safe mechanism in the septal ring assembly pathway generated by the sequential recruitment of cell separation amidases and their activators. *J. Bacteriol.* **193**, 4973–4983 (2011).
15. C. Heidrich, A. Ursinus, J. Berger, H. Schwarz, J. V. Höltje, Effects of multiple deletions of murein hydrolases on viability, septum cleavage, and sensitivity to large toxic molecules in *Escherichia coli*. *J. Bacteriol.* **184**, 6093–6099 (2002).
16. A. I. Weaver *et al*., Lytic transglycosylases RlpA and MltC assist in *Vibrio cholerae* daughter cell separation. *Mol. Microbiol.* **112**, 1100–1115 (2019).
17. R. Priyadarshini, M. A. de Pedro, K. D. Young, Role of peptidoglycan amidases in the development and morphology of the division septum in *Escherichia coli*. *J. Bacteriol.* **189**, 5334–5347 (2007).
18. R. Priyadarshini, D. L. Popham, K. D. Young, Daughter cell separation by penicillin-binding proteins and peptidoglycan amidases in *Escherichia coli*. *J. Bacteriol.* **188**, 5345–5355 (2006).
19. A. Möll *et al*., Cell separation in *Vibrio cholerae* is mediated by a single amidase whose action is modulated by two nonredundant activators. *J. Bacteriol.* **196**, 3937–3948 (2014).
20. E. Scheurwater, C. W. Reid, A. J. Clarke, Lytic transglycosylases: Bacterial space-making autolysins. *Int. J. Biochem. Cell Biol.* **40**, 586–591 (2008).
21. E. M. Scheurwater, L. L. Burrows, Maintaining network security: How macromolecular structures cross the peptidoglycan layer. *FEMS Microbiol. Lett.* **318**, 1–9 (2011).
22. F. A. Herlihey, A. J. Clarke, Controlling autolysis during flagella insertion in gram-negative bacteria. *Adv. Exp. Med. Biol.* **925**, 41–56 (2017).
23. T. Dörr, F. Cava, H. Lam, B. M. Davis, M. K. Waldor, Substrate specificity of an elongation-specific peptidoglycan endopeptidase and its implications for cell wall architecture and growth of *Vibrio cholerae*. *Mol. Microbiol.* **89**, 949–962 (2013).
24. S. K. Singh, L. SaiSree, R. N. Amrutha, M. Reddy, Three redundant murein endopeptidases catalyse an essential cleavage step in peptidoglycan synthesis of *Escherichia coli* K12. *Mol. Microbiol.* **86**, 1036–1051 (2012).
25. M. Hashimoto *et al*., Digestion of peptidoglycan near the cross-link is necessary for the growth of *Bacillus subtilis*. *Microbiology* **164**, 299–307 (2018).
26. M. Hashimoto, S. Ooiwa, J. Sekiguchi, Synthetic lethality of the lytE cwlO genotype in *Bacillus subtilis* is caused by lack of D,L-endopeptidase activity at the lateral cell wall. *J. Bacteriol.* **194**, 796–803 (2012).
27. T. Dörr, B. M. Davis, M. K. Waldor, Endopeptidase-mediated beta lactam tolerance. *PLoS Pathog.* **11**, e1004850 (2015).
28. H. Cho, T. Uehara, T. G. Bernhardt, Beta-lactam antibiotics induce a lethal malfunctioning of the bacterial cell wall synthesis machinery. *Cell* **159**, 1300–1311 (2014).
29. T. Uehara, T. Dinh, T. G. Bernhardt, LytM-domain factors are required for daughter cell separation and rapid ampicillin-induced lysis in *Escherichia coli*. *J. Bacteriol.* **191**, 5094–5107 (2009).
30. K. Kitano, E. Tuomanen, A. Tomasz, Transglycosylase and endopeptidase participate in the degradation of murein during autolysis of *Escherichia coli*. *J. Bacteriol.* **167**, 759–765 (1986).
31. L. G. Monahan *et al*., Rapid conversion of *Pseudomonas aeruginosa* to a spherical cell morphotype facilitates tolerance to carbapenems and penicillins but increases susceptibility to antimicrobial peptides. *Antimicrob. Agents Chemother.* **58**, 1956–1962 (2014).
32. T. Cross *et al*., Spheroplast-mediated carbapenem tolerance in Gram-negative pathogens. *Antimicrob. Agents Chemother.* **63**, e00756-19 (2019).
33. P. K. Chodisetti, M. Reddy, Peptidoglycan hydrolase of an unusual cross-link cleavage specificity contributes to bacterial cell wall synthesis. *Proc. Natl. Acad. Sci. U.S.A.* **116**, 7825–7830 (2019).
34. J. van Heijenoort, Peptidoglycan hydrolases of *Escherichia coli*. *Microbiol. Mol. Biol. Rev.* **75**, 636–663 (2011).
35. J. Meisner *et al*., FtsEX is required for CwlO peptidoglycan hydrolase activity during cell wall elongation in *Bacillus subtilis*. *Mol. Microbiol.* **89**, 1069–1083 (2013).
36. P. Domínguez-Cuevas, I. Porcelli, R. A. Daniel, J. Errington, Differentiated roles for MreB-actin isologues and autolytic enzymes in *Bacillus subtilis* morphogenesis. *Mol. Microbiol.* **89**, 1084–1098 (2013).
37. Y. R. Brunet, X. Wang, D. Z. Rudner, SweC and SweD are essential co-factors of the FtsEX-CwlO cell wall hydrolase complex in *Bacillus subtilis*. *PLoS Genet.* **15**, e1008296 (2019).
38. L. I. Salzberg, J. D. Helmann, An antibiotic-inducible cell wall-associated protein that protects *Bacillus subtilis* from autolysis. *J. Bacteriol.* **189**, 4671–4680 (2007).
39. P. Bisicchia *et al*., The essential YycFG two-component system controls cell wall metabolism in *Bacillus subtilis*. *Mol. Microbiol.* **65**, 180–200 (2007).
40. M. Banzhaf, The outer membrane lipoprotein NlpI nucleates hydrolases within peptidoglycan multi-enzyme complexes in *Escherichia coli*. bioRxiv:10.1101/609503 (16 April 2019).
41. D. C. Yang *et al*., A genome-wide *Helicobacter pylori* morphology screen uncovers a membrane-spanning helical cell shape complex. *J. Bacteriol.* **201**, e00724-18 (2019).
42. S. G. Murphy *et al*., Endopeptidase regulation as a novel function of the zur-dependent zinc starvation response. *MBio* **10**, e02620-18 (2019).
43. Z. R. Lonergan *et al*., An Acinetobacter baumannii, zinc-regulated peptidase maintains cell wall integrity during immune-mediated nutrient sequestration. *Cell Rep.* **26**, 2009–2018.e6 (2019).
44. D. Srivastava *et al*., A proteolytic complex targets multiple cell wall hydrolases in *Pseudomonas aeruginosa*. *MBio* **9**, e00972-18 (2018).
45. S. K. Singh, S. Parveen, L. SaiSree, M. Reddy, Regulated proteolysis of a cross-link-specific peptidoglycan hydrolase contributes to bacterial morphogenesis. *Proc. Natl. Acad. Sci. U.S.A.* **112**, 10956–10961 (2015).
46. S. Ragumani, D. Kumaran, S. K. Burley, S. Swaminathan, Crystal structure of a putative lysostaphin peptidase from *Vibrio cholerae*. *Proteins* **72**, 1096–1103 (2008).
47. X. Wang *et al*., Crystal structure of outer membrane protein NMB0315 from *Neisseria meningitidis*. *PLoS One* **6**, e26845 (2011).
48. D. R. An *et al*., Structure of Csd3 from *Helicobacter pylori*, a cell shape-determining metallopeptidase. *Acta Crystallogr. D Biol. Crystallogr.* **71**, 675–686 (2015).
49. G. Buist, A. Steen, J. Kok, O. P. Kuipers, LysM, a widely distributed protein motif for binding to (peptido)glycans. *Mol. Microbiol.* **68**, 838–847 (2008).
50. M. Grabowska, E. Jagielska, H. Czapinska, M. Bochtler, I. Sabala, High resolution structure of an M23 peptidase with a substrate analogue. *Sci. Rep.* **5**, 14833 (2015).
51. C. F. Schierle *et al*., The DsbA signal sequence directs efficient, cotranslational export of passenger proteins to the *Escherichia coli* periplasm via the signal recognition particle pathway. *J. Bacteriol.* **185**, 5706–5713 (2003).
52. T. D. Grant, Ab initio electron density determination directly from solution scattering data. *Nat. Methods* **15**, 191–193 (2018).
53. A. Waterhouse *et al*., SWISS-MODEL: Homology modelling of protein structures and complexes. *Nucleic Acids Res.* **46**, W296–W303 (2018).
54. G. C. Lai, H. Cho, T. G. Bernhardt, The mecillinam resistome reveals a role for peptidoglycan endopeptidases in stimulating cell wall synthesis in *Escherichia coli*. *PLoS Genet.* **13**, e1006934 (2017).
55. B. Ostash, S. Walker, Moenomycin family antibiotics: Chemical synthesis, biosynthesis, and biological activity. *Nat. Prod. Rep.* **27**, 1594–1617 (2010).

56. A. W. Bauer, D. M. Perry, W. M. Kirby, Single-disk antibiotic-sensitivity testing of staphylococci; an analysis of technique and results. *AMA Arch. Intern. Med.* **104**, 208–216 (1959).
57. N. Bernardo-García *et al*., Allostery, recognition of nascent peptidoglycan, and cross-linking of the cell wall by the essential penicillin-binding protein 2x of *Streptococcus pneumoniae*. *ACS Chem. Biol.* **13**, 694–702 (2018).
58. L. H. Otero *et al*., How allosteric control of *Staphylococcus aureus* penicillin binding protein 2a enables methicillin resistance and physiological function. *Proc. Natl. Acad. Sci. U.S.A.* **110**, 16808–16813 (2013).
59. M. Lee *et al*., Exolytic and endolytic turnover of peptidoglycan by lytic transglycosylase Slt of *Pseudomonas aeruginosa*. *Proc. Natl. Acad. Sci. U.S.A.* **115**, 4393–4398 (2018).
60. T. Domínguez-Gil *et al*., Activation by allostery in cell-wall remodeling by a modular membrane-bound lytic transglycosylase from *Pseudomonas aeruginosa*. *Structure* **24**, 1729–1741 (2016).
61. A. Amir, D. R. Nelson, Dislocation-mediated growth of bacterial cell walls. *Proc. Natl. Acad. Sci. U.S.A.* **109**, 9833–9838 (2012).
62. L. G. Burman, J. T. Park, Molecular model for elongation of the murein sacculus of *Escherichia coli*. *Proc. Natl. Acad. Sci. U.S.A.* **81**, 1844–1848 (1984).
63. G. W. Li, D. Burkhardt, C. Gross, J. S. Weissman, Quantifying absolute protein synthesis rates reveals principles underlying allocation of cellular resources. *Cell* **157**, 624–635 (2014).
64. D. C. Yang, K. Tan, A. Joachimiak, T. G. Bernhardt, A conformational switch controls cell wall-remodelling enzymes required for bacterial cell division. *Mol. Microbiol.* **85**, 768–781 (2012).
65. A. L. Koch, Additional arguments for the key role of "smart" autolysins in the enlargement of the wall of gram-negative bacteria. *Res. Microbiol.* **141**, 529–541 (1990).
66. J. F. Heidelberg *et al*., DNA sequence of both chromosomes of the cholera pathogen *Vibrio cholerae*. *Nature* **406**, 477–483 (2000).
67. D. G. Gibson *et al*., Enzymatic assembly of DNA molecules up to several hundred kilobases. *Nat. Methods* **6**, 343–345 (2009).
68. M. S. Donnenberg, J. B. Kaper, Construction of an eae deletion mutant of enteropathogenic *Escherichia coli* by using a positive-selection suicide vector. *Infect. Immun.* **59**, 4310–4317 (1991).
69. Z. Otwinowski, W. Minor, Processing of X-ray diffraction data collected in oscillation mode. *Methods Enzymol.* **276**, 307–326 (1997).
70. S. Trapani, J. Navaza, AMoRe: Classical and modern. *Acta Crystallogr. D Biol. Crystallogr.* **64**, 11–16 (2008).
71. P. Emsley, B. Lohkamp, W. G. Scott, K. Cowtan, Features and development of Coot. *Acta Crystallogr. D Biol. Crystallogr.* **66**, 486–501 (2010).
72. G. N. Murshudov *et al*., REFMAC5 for the refinement of macromolecular crystal structures. *Acta Crystallogr. D Biol. Crystallogr.* **67**, 355–367 (2011).
73. C. Vonrhein *et al*., Data processing and analysis with the autoPROC toolbox. *Acta Crystallogr. D Biol. Crystallogr.* **67**, 293–302 (2011).
74. A. J. McCoy *et al*., Phaser crystallographic software. *J. Appl. Cryst.* **40**, 658–674 (2007).
75. P. D. Adams *et al*., PHENIX: A comprehensive python-based system for macromolecular structure solution. *Acta Crystallogr. D Biol. Crystallogr.* **66**, 213–221 (2010).